Model-assisted analysis and prediction of activity degradation in PEM-fuel cell cathodes

David Bernhard [a,c], Thomas Kadyk [b,*], Sebastian Kirsch [a,*], Hannes Scholz [a], Ulrike Krewer [c]

[a] *Volkswagen AG, Berliner Ring 2, 38440 Wolfsburg, Germany*
[b] *Institute of Energy and Climate Research, Theory and Computation of Energy Materials (IEK-13), Forschungszentrum Jülich GmbH, 52425 Jülich, Germany*
[c] *Institute for Applied Materials - Electrochemical Technologies (IAM-ET), Karlsruhe Institute of Technology, Adenauerring 20b, 76131 Karlsruhe, Germany*

HIGHLIGHTS

- Catalyst activity is described by Tafel slope and exchange current density.
- Catalyst activity correlates with changing ECSA.
- The presented model consists of two submodels: 1st model describes ECSA loss.
- 2nd model: prediction of voltage losses across a wide range of AST parameters.
- Voltage losses are dominated by the change of Tafel slope, not by the loss of ECSA.

ARTICLE INFO

ABSTRACT

This work presents a model for the prediction and analysis of voltage losses in proton exchange membrane fuel cells arising from accelerated stress testing. It consists of two submodels. The first submodel uses a statistical physics-based population balance approach to describe the degradation of the catalyst active surface. It is combined with a performance submodel that allows incorporating the degradation of the catalyst activity. During testing, a dedicated diagnostic procedure is used to determine the cell performance and the cathode properties, like the electrochemical active surface area, during the stress tests. It was found that the change of the catalyst activity, described by Tafel slope and exchange current density, correlates with the change in active surface area. The model allows the description of catalyst surface reduction, changes of Tafel slope and exchange current density as well as voltage losses. We find that the voltage losses attributed to the loss of electrochemical active surface area are minor, while the dominant factor is the change of the Tafel-slope. Accordingly, this study shows that during PEM-FC cathode degradation studies the Tafel slope should be the most relevant metric. The model describes the experimental data with a standard deviation of 7.1 mV in a range of 0–2.0 A/cm^2. The model is intended to be used as a building block for the prediction of performance losses of PEM fuel cells under drive cycle conditions.

1. Introduction

In view of climate change and an increasing uncertainty in the energy market, hydrogen is becoming increasingly important as emission free energy source for stationary and mobility applications [1 3]. Polymer Electrolyte Fuel Cells (PEM FCs) are currently the best option to convert H_2 into propulsion energy to drive passenger cars, trucks, trains or even planes. Due to the higher well to wheel efficiency, batteries have an advantage in operating costs in these transport sectors. But as batteries come with more weight, more cost (at least for long ranges) and longer charging times, PEM FCs have a good chance to have their market share as soon as H_2 becomes available, especially for heavy duty vehicles (HDV) [3,4]. Nevertheless, PEM FCs in HDV face the same or even greater technical challenges as in light duty vehicles (LDVs). For example, the US Department of Energy lifetime target for hydrogen Class 8 long haul trucks in 2030 is 25.000 h with an ultimate target of as much as 30.000 h [3,5 7], compared to LDV with 8.000 h. Consequently, degradation is still one of the major challenges to make PEM FCs in automotive applications commercially competitive [3,4,6 8].

Especially cathode degradation must be managed, as catalytic activity losses and losses of the electrochemically active surface area (ECSA)

are the dominant sources of performance loss [4,9 15]. The losses are linked to different degradation mechanisms. Losses of ECSA are related to (1) platinum dissolution and redeposition, (2) precipitation of dissolved platinum ions in the adjacent membrane, (3) coagulation or (4) loss of catalyst particles due to the corrosion of the carbon support material [16 20]. Losses of catalytic activity arise in consequence of structural changes such as distributions of particle sizes and particle facets, and of changes in composition, if alloy materials are used [21 29]. The catalytic activity for the oxygen reduction reaction (ORR) can be described by using the Tafel kinetic approach with the parameters Tafel slope and exchange current density [10,24,30,31]. For pure plat inum catalysts these parameters are often assumed as constant over PEM FC cathode lifetime [13,15,32]. However, changes of the Tafel slope and the exchange current density are significant, as highlighted recently [10]. While some works show that in the course of degra dation, the Tafel slope increased for Pt based cathodes, Arisetty et al. found an increasing exchange current density [21]. Not unexpectedly, changes in Tafel slope and exchange current density were also found during the degradation of alloy catalysts [33,34].

A variety of accelerated stress tests (ASTs), like triangular wave or square wave ASTs, are used in literature to produce an electrode state close to the end of life (EoL) state targeted in LDV or HDV application. In a number of works, different stressors, controlled by the operating parameters of the AST, such as potential, waveform, hold times, temperature and relative humidity on catalyst degradation are studied [9,12,13,15,35]. Such data is specifically relevant for the development and validation of degradation models of PEM FCs.

Generally, the variety of different degradation model approaches can be divided into empirical approaches, physical approaches and hybrid approaches combining empirical and physical equations. In the group of the empirical approaches, data driven modeling has recently gained more interest [36 40]. A summary of models that make use of artificial intelligence like neural networks or machine learning is given in [41 43]. These models gain their predictive capabilities from analyzing large sets of data [40,41]. But as large amount of degradation and performance data are rare, the applicability of these approaches is limited. Further empirical approaches dealing with degradation and performance losses in PEM FCs can be found in literature [8,44 48]. For example, Chen et al. [45] assigned data from fuel cell buses to four alternative operating modes. For these operating modes, the voltage loss per start stop and load change cycles or per hour for idling and high power load phases is determined. By summing up these losses, the performance loss can be predicted. With this approach, Chen et al. were able to predict the voltage loss for their PEM FC stack for arbitrary drive cycles. However, the applicability to other PEM FC systems or operating conditions lacks generalizability. The model published by Messing et al. [8] used a start stop AST and a load cycling AST with harsh conditions. They derived two equations to describe the voltage loss caused by the two distinct ASTs. Then, they deconvoluted drive cycles into a series of start stop and load cycling ASTs. With this approach, they were able to predict the run time under different drive cycle scenarios until 90% of the starting voltage at 0.6 A/cm² is reached. Unfortunately, the impact of changes in temperature, relative humidity and pressure is not considered, even though the operating conditions can have a significant influence on the cathode degradation [12,28,49 53].

In contrast to empirical models, physical mathematical models are used to describe changes of the cathode catalyst [11,12,52,54 59]. For example, Holby et al. derived a kinetic platinum dissolution model to describe ECSA losses. These losses are related to a change of the particle size distribution (PSD) [54]. Li et al. refined this model by adding Ostwald ripening, platinum precipitation in the ionomer and the membrane [57]. A further model that uses the PSD changes to predict ECSA losses is presented by Schneider et al. [12]. Their model accounts for Pt in the membrane, Ostwald ripening, the loss of catalyst particles caused by carbon corrosion and the loss of platinum due to

the formation of subsurface oxides at potentials of >1.1 V. Further PSD based degradation models can be found in [11,52,58 63]. While these models are very useful to describe one part of catalyst degradation, namely ECSA loss, to the best of our knowledge, no physical models exists to describe the other part, namely losses of catalyst activity (measured by Tafel slope and exchange current density). Accordingly, the derivation of cell voltage losses based on Tafel kinetics lacks precision when only ECSA losses are considered. From this perspective the voltage loss should be independent of current density, whereby it typically increases.

Alternatively, catalyst degradation and linked voltage losses can be described with semi empirical approaches [13,64 68]. For example, Moein Jahromi et al. used an empirical model approach to describe the decay of ECSA, which is based on a first order ECSA decline rate. This loss of active surface is converted into a PSD, to derive the surface for oxygen diffusion through the ionomer film surrounding the catalyst particles. In addition, they have developed a physics based performance prediction model, which uses ECSA and the surface for oxygen diffusion as input parameters [69]. Another semi empirical approach is presented by Kneer et al. [13]. They derived an empirical ECSA loss model, based on a first order kinetic approach, that is capable to predict the ECSA loss for a wide range of AST parameters. These losses are then used as input for their performance loss prediction model that is based on simple Tafel kinetics. With this model they are able to predict the voltage loss up to a current density of 1.5 A/cm² reasonably. However, also here the dependence on current density is lacking as a consequence of ignoring the changes in the other kinetic parameters.

For the design of durable fuel cell systems, models are needed, which allow the prediction of degradation related performance losses under drive cycle scenarios and related operating conditions. A possible approach is to convert drive cycles into an equivalent series of accel erated stress tests. Accordingly, the main objective of this work is to enable the performance loss prediction for accelerated stress test under various operating conditions like voltage profile or temperature.

One suitable model, capable to predict the loss of the electro chemical active surface area and the related performance losses for pure platinum catalysts aged with accelerated stress test with various operating conditions is the one presented in [13]. Our work extends this approach by enabling predictions of Tafel slope, exchange current density and consequently performance losses in PEM fuel cells.

The first part of the model is formed by a statistical physical model for particle radius distribution (PRD) evolution and ECSA loss [55]. The model is extended to account for the impact of the most important AST parameter dependencies. By analyzing the experimental data, cor relations were found between the ECSA loss on the one side, and Tafel slope as well as specific exchange current density on the other side. These observed changes of Tafel slope and specific exchange current density are related to the different catalyst degradation mechanism like dealloying and changes in the distribution of the crystal facets. Accordingly, the second part of the model, bases on an extended Tafel kinetic approach that accounts for these correlations and allows to predict cell voltage losses. After global parametrization, the model allows to reproduce the voltage losses, measured in a current density range of 0.0 2.0 A/cm² with an accuracy of 7.1 mV.

2. Experimental

2.1. Materials and equipment

The size of the active area during single cell testing was 5 cm², with flowfields made of graphite and a flowfield design based on studies of Caulk and Baker (shown in the supplementary material (A) [70]. The catalyst coated membrane had a loading of 0.25 mg_Pt/cm² PtCo cathode catalyst with a Pt:Co molar ratio of 70:30 in the raw powder, an un alloyed Pt anode with a loading of 0.05 mg_Pt/cm², an ionomer in both electrodes with a low equivalent weight, and a persulfonic

Table 1
Overview of the varying conditions during accelerated test aging of the fuel cells.

AST-type	LPL [V]	UPL [V]	T [°C]	RH [%]	τ [s][a]	n_{EoT}
1 (Ref.)	0.6	OCV[b] (~0.98)	90	100	5	63500
2	0.72	OCV	90	100	5	63500
3	0.6	OCV	90	100	20	31500[c]
4	0.6	OCV	90	100	2.5	63500
5	0.6	OCV	70	100	5	63500
6	0.6	OCV	90	80	5	63500
7	0.6	0.85	90	100	5	63500
8	0.6	0.85	80	52.4	5	63500
9	0.6	0.9	90	100	10	31500[d]
10	0.6	0.9	90	100	2.5	63500

[a]Describes the hold time at the lower potential limit (LPL) and upper potential limit (UPL).
[b]Open circuit voltage.
[c]AST stopped after 31500 cycles as $ECSA_{norm} < 0.5$ is reached.
[d]AST stopped after 31500 cycles due to technical problems.

acid based membrane with a thickness of 18 µm. Sigracet 25BC gas diffusion layers were used on both electrodes, compressed with a pneumatic hardware to 1 MPa in the active area. All electrochemical data and operation conditions were gathered with a fully automatized test bench from Horiba FuelCon and an additional external Zahner Zennium potentiostat.

2.2. Testing

The basic test sequence consists of four parts. It begins with a conditioning procedure, consisting of several step changes in current and voltage, to activate the membrane electrode assemblies (MEAs). Afterwards, the MEAs were characterized at begin of life (BoL) with a developed diagnostic procedure, containing cyclic voltametry to determine the ECSA and an extended polarization curve measurement between 0.0 2.0 A/cm². For every single load point of the polarization curve, the limiting current measurement and electrochemical impedance spectra (EIS) between 50 Hz and 30 kHz were recorded to determine the oxygen mass transport resistance (R_{mt}) respectively, the high frequency resistance (R_{HFR}) and the proton transport resistance (R_{H^+}). Exemplary data sets are given in the supplementary material B. The operation conditions used in the diagnostic procedure and a detailed description of this procedure can be found in [9]. After the diagnostic procedure, the MEAs were degraded with accelerated stress tests. These tests were stopped when 50 % loss of ECSA or 63,500 AST cycles were reached. The diagnostic procedure was repeated to characterize the MEAs within the AST and at end of test (EoT). The ASTs and the extended polarization curve measurements were carried out with an air and H$_2$ flow of 5 Nl/min and an inlet pressure on both sides of 2 bar, to ensure that the cell is working under differential conditions. Thus, cell temperature, pressure and relative humidity can be assumed to be constant over the active area of 5 cm². The parameters for the individual square wave ASTs are listed in Table 1.

ASTs 1, 3 and 4 are used to analyze the influence of the hold times at the potential limits on the degradation behavior of the MEA used. In AST 1 and AST 2, the lower potential limit (LPL) is varied in order to determine the influence of ASTs with two distinct LPLs on the catalyst used. ASTs 1 and 7 are used to analyze the influence of the upper potential limit (UPL) on the degradation of the catalyst. With ASTs 1 and 5, it was determined how degradation is impacted by the temperature, and with ASTs 1, 7 and 8 the impact of relative humidity (RH) is investigated.

2.3. Determination of kinetic cathode losses

Kinetic cathode losses are understood as voltage losses in absence of Ohmic losses (majorly from membrane and cathode ionomer), losses

from oxygen transport. Anodic losses are generally assumed to be negligible. By correcting the measured cell voltage with these overpotentials, the cathodic half cell voltage E_C can be calculated with Eq. (1)

$$E_C(n,i) = U_{Cell}(n,i) + \eta_{R_{HFR}}(n,i) + \eta_{mt}(n,i) + \eta_{R_{H^+}}(n,i), \quad (1)$$

where $U_{Cell}(n,i)$ represents the measured cell voltage depending at the number of AST cycles n and the current density i [10,71]. The second, third and fourth term on the right hand side of Eq. (1) describe the overpotentials related to the Ohmic resistance determined by R_{HFR}, the oxygen mass transport determined by R_{mt} and the transport of the protons through the catalyst ionomer determined by R_{H^+}. The Ohmic overpotential, linked to the high frequency resistance, can be calculated with

$$\eta_{R_{HFR}}(n,i) = i \cdot A \cdot R_{HFR}(n,i), \quad (2)$$

where A describes the active area of the MEA (5 cm²). The second overpotential in Eq. (1) related to the oxygen mass transport behavior of the MEA, can be calculated with [15]

$$\eta_{mt}(n,i) = \frac{R \cdot T}{F} \cdot \left(\frac{1}{4} + \frac{\gamma}{\alpha}\right) \cdot 10^3 \frac{mV}{V} \cdot ln\left(\frac{p_{O2} - \frac{R \cdot T}{4F} \cdot i \cdot R_{mt}(n,i) \cdot 10^6 \frac{cm^3}{m^3}}{p_{O2}}\right), \quad (3)$$

where α represents the cathodic transfer coefficient obtained from the Tafel slope, γ is the ORR reaction order with respect to oxygen partial pressure ($\gamma = 0.54$ according to [32])and p_{O2} is the oxygen partial pressure in the channels of the flow field. According to Makharia et al. [72] the third overpotential is calculated by using the proton transport resistance of the cathode ionomer R_{H^+}

$$\eta_{R_{H^+}}(n,i) = \frac{1}{3} \cdot i \cdot A \cdot R_{H^+}(n,i), \quad (4)$$

Half cell voltages $E_C(n,i)$ over the course of AST testing can be seen in Section 4.1(see Fig. 3a). The half cell voltages are also used to derive the slope m and the exchange current density i_0 by extrapolating the polarization curves between 0.04 and 0.12 A/cm² to the reversible cell voltage (1.18 V).

3. Modeling

In the following, the model equations describing the ECSA loss (Section 3.1) and the voltage loss prediction (see Section 3.2) are introduced. Afterwards, an exemplary simulation is presented to visualize the mechanics of the models (see Section 3.3).

3.1. Losses in electrochemical surface area

The variable to track the degradation of the electrode catalyst is the particle radius distribution $f_N(r,t)$, which is normalized to the begin of

life particle radius distribution. According to Urchaga et al. the change of the distribution over time can be described by a Fokker Planck type continuity equation, where the particle radius distribution (PRD) is described by using the particle radius r [55],

$$\frac{\partial f_N(r,t)}{\partial t} = \frac{\partial}{\partial r} \cdot \left(f_N(r,t) \cdot \frac{dr}{dt} \right) + J^+ - J^- - k_{det} \cdot f_N(r,t). \tag{5}$$

In this equation, the first term on the right hand side describes the dissolution and redeposition due to Ostwald ripening. The terms J^+ and J^- describe particle coagulation and represent the particle creation and extinction terms, respectively. The last term describes particle in activation, e.g. by detachment from the substrate. By trying to identify J^+ and J^- in the individual AST data sets we ran into the problem of overfitting and in consequence we neglected these contributions.[1] Accordingly, the change in particle radius distribution can be described with

$$\frac{\partial f_N(r,t)}{\partial t} = \frac{\partial}{\partial r} \cdot \left(f_N(r,t) \cdot \frac{dr}{dt} \right). \tag{6}$$

The rate of particle radius change is determined by dissolution and redeposition terms [55],

$$\frac{dr}{dt} = V_m \cdot k_{rdp} \cdot \bar{c}_{Pt}(t) \cdot exp\left(\frac{-R_0}{r} \right) - V_m \cdot k_{dis} \cdot c_{Pt}^{ref} \cdot exp\left(\frac{R_0}{r} \right), \tag{7}$$

where the redeposition parameter k_{rdp}, the product of dissolution parameter and platinum concentration $k_{dis} \cdot c_{Pt}^{ref}$ and the characteristic radius R_0 are extracted from the measured ECSA evolution depending on the AST conditions summarized in Table 2. Note that we use two different rate constants k_{dis} and k_{rdp} for forward and backward reaction. The Pt redeposition rate depends on the concentration of Pt dissolved in the electrolyte, which can be calculated as [55]

$$\bar{c}_{Pt}(t) = \frac{m_V}{M_{Pt}} \cdot \left(1 - M_N(t) \right) \tag{8}$$

assuming that the initial concentration is zero, $\bar{c}_{Pt}(t = 0) = 0$. Here, m_V is the Pt mass loading per unit volume, $M_{P}t$ is the molecular weight of Pt and $M_N(t)$ is the normalized dimensionless mass moment of $f_N(r,t)$ [55].

$$M_N(t) = \frac{\int_0^\infty r^3 \cdot f_N(r,t) dr}{\int_0^\infty r^3 \cdot f_N(r,0) dr} \tag{9}$$

Solving Eq. (6), using Eq. (7), allows the determination of the evolution of the normalized electrochemical active surface area $ECSA_{norm}$ [55],

$$ECSA_{norm}(t) = \frac{\int_0^\infty r^2 \cdot f_N(r,t) dr}{\int_0^\infty r^2 \cdot f_N(r,0) dr}. \tag{10}$$

The model is solved by using a variable order solver based on numerical differentiation formulas implemented as ODE15s in MATLAB version 9.5.0.944444 (R2018b). The three parameters k_{rdp}, $k_{dis} \cdot c_{Pt}^{ref}$ and R_0 were fitted with a least squares method. For the minimization a Nelder Mead simplex algorithm was implemented (Used MATLAB function: fminsearch).

The evolution of the ECSA depends on the operating conditions of the AST. Empirical relationships between the degradation parameters and operating conditions were derived. More information are given in the supplementary material C. In Eqs. (11) and (12) the derived relationship between the dissolution related parameter $k_{dis} \cdot c_{Pt}^{ref}$, respectively the redeposition related parameter k_{rdp} and the AST conditions

Table 2
Overview parameters ECSA-Model (see equations (11) and (12)).

Parameter		Unit
R_0	22.039	[nm]
$c_{Pt}^{ref} k_{dis}$	$1.9909 \cdot 10^{-16}$	[mol/m^{2}s]
g_τ	0.0728	[1/s]
g_T	4875.7	[K]
g_{LPL}	2.6930	[1/V]
g_{UPL}	12.8143	[1/V]
g_{RH}	1.1644	[–]
$k_{rdp,ref}$	$1.9900 \cdot 10^{-10}$	[m/s]
h_τ	0.3446	[1/s]
h_{UPL}	28.8074	[1/V]
T_{ref}	363.15	[K]
τ_{ref}	5	[s]
LPL_{ref}	0.6	[V]
UPL_{ref}	OCV(~0.98)	[V]
RH_{ref}	100	[%]

are shown,

$$c_{Pt}^{ref} \cdot k_{dis}(UPL, LPL, RH, T, \tau) = c_{Pt}^{ref} k_{dis,ref} \cdot \left(1 + g_\tau \cdot (\tau - \tau_{ref}) \right)$$
$$\cdot exp\left(-g_T \cdot \left(\frac{1}{T} - \frac{1}{T_{ref}} \right) \right)$$
$$\cdot exp\left(g_{LPL} \cdot (LPL - LPL_{ref}) \right) \tag{11}$$
$$\cdot exp\left(g_{UPL} \cdot (UPL - UPL_{ref}) \right)$$
$$\cdot \left(1 + g_{RH} \cdot \left(\frac{RH}{RH_{ref}} - 1 \right) \right)$$

and

$$k_{rdp}(\tau, UPL) = k_{rdp,ref} \cdot exp(h_\tau \cdot (\tau - \tau_{ref})) \cdot exp(-h_{UPL} \cdot (UPL - UPL_{ref})). \tag{12}$$

The parameters $c_{Pt}^{ref} k_{dis,ref}, g_\tau, g_T, g_{LPL}, g_{UPL}$ and g_{RH}, respectively $k_{rdp,ref}, h_\tau$ and h_{UPL} are needed to describe the dependency of the degradation parameters $k_{dis} \cdot c_{Pt}^{ref}$ and k_{rdp} from the operation conditions of the AST. The identified parameters and the reference values are summarized in Table 2.

3.2. Kinetic voltage losses

Assuming that Tafel slope and exchange current density can be correlated uniquely to the cycle number n of a given AST (see Section 4.3 for proof), the cathode overpotential E_C can be understood via a generalized Tafel approach

$$E_C(n, i) = m(n) \cdot log\left(\frac{i}{i_0(n) \cdot ECSA(n)} \right), \tag{13}$$

with m being the tafel slope and i_0 the exchange current density. The kinetic cathode voltage losses arising from AST testing then follow from

$$\Delta E_C(n, i) = m(n) \cdot log\left(\frac{i}{i_0(n) \cdot ECSA(n)} \right)$$
$$- m(0) \cdot log\left(\frac{i}{i_0(0) \cdot ECSA(0)} \right). \tag{14}$$

According to Eqs. (14), at least two further functions are needed to describe $i_0(n)$ and $m(n)$. In Section 4.3 two empirical correlations are introduced, which can be used to describe the change of these two cathode parameters.

3.3. Modeling process

Fig. 1 gives a visual impression of the model and its mechanics for an exemplary data set based on the degradation conditions of AST 1

---

[1] This simplification of Eq. (5) is justified, as degradation of the cathode catalyst due to coagulation and inactivation of the catalyst particles is mainly driven by carbon corrosion [43,73,74]. Significant corrosion rates are normally expected at cell voltages higher than 1 V [10,75–77], which do not occur in the degradation experiments carried out in this work.
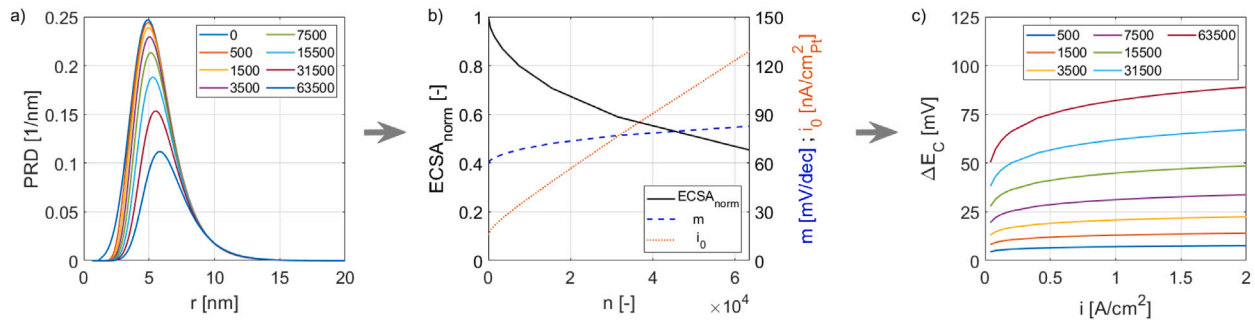
Fig. 1. Model process shown with a exemplary data set based on the operation conditions of AST 1 defined in Table 1: (a) Evolution of the normalized particle radius distribution (surface scaled) with cycle number given in the legend; (b) Evolution of the normalized $ECSA$ derived from the PSDs shown in (a) and the simulated values for m and i_0 depending on the number of AST cycles n; (c) Kinetic voltage losses ΔE_C between 0.0–2.0 A/cm^2 calculated with $ECSA_{norm}$, m and i_0 shown in (b).

(see Table 1). Fig. 1a shows the simulated evolution of the PRD for the catalyst used under the operating conditions of AST 1. It can be seen that the PRD is shifted to larger particle radii with increasing number of AST cycles and ongoing degradation. The black line in Fig. 1b represents the ECSA evolution based on Eq. (10). The simulated values for m and i_0 (the empirical correlations with Eq. (15) and (16) are presented below) depending on the number of AST cycles n are shown in Fig. 1b. In Fig. 1c, the voltage losses ΔE_C in the current density range from 0.0 2.0 A/cm^2 are shown, calculated with the generalized Tafel approach.

4. Results and discussion

In the following, we first analyze the experimentally determined trends of key variables for the different AST conditions summarized in Table 1. The key variables are ECSA, Tafel slope, exchange current density and cathode kinetic loss (see Section 4.1). In Section 4.2, the results obtained with the surface loss model introduced in Sec tion 3.1 are shown and discussed. Subsequently, empirical correlations describing the Tafel slope and exchange current density as function of the normalized ECSA are derived and the parameters describing these correlations are identified (see Section 4.3). Finally, the accuracy of the kinetic cathode voltage loss model is discussed in Section 4.4.

4.1. Evaluation of experimental data

Fig. 2 displays the influence of the different AST conditions on the measured ECSA loss. Fig. 2a shows the influence of the UPL variation (0.85 V vs. OCV). It can be seen that with an UPL of 0.85 V, an ECSA loss of 15% is reached after 3.000 AST cycles. Afterwards, the ECSA loss decreases and an almost asymptotic behavior can be observed. Contrary with an UPL of 0.98 V, the ECSA is continuously reduced and no asymptotic behavior can be observed within the first 30,000 AST cycles. Overall, there is a reduction to 55% of ECSA for 0.98 V vs. 83% for 0.85 V. This result is in line with the findings presented in [10,12 15,78 80]. In Fig. 2b, the influence of the hold time is presented. It can be seen, that the ECSA loss increases with increasing hold time of the potential limits. After 31,500 AST cycles, the ECSA is reduced by 33%, 45% and 64% of the original ECSA for hold time τ of 2.5 s, 5 s respectively 20 s. Comparable trends were observed earlier [10,12,13,15,78]

In Fig. 2c, the influence of T, RH and LPL on the measured ECSA loss is shown. Again, the ECSA decay of AST 1 is used as reference (blue line in 2a c). It can be seen that an increase of the LPL to 0.72 V has no significant influence on the ECSA loss, comparable to observations of Kneer et al. [13]. Reducing the temperature by about 20 K reduces the ECSA loss after 31,500 AST cycles by about 20%. A decreased degradation due to a temperature reduction has been also reported in [12,49 52]. Similarly, a reduction of the relative humidity causes a slight decrease of the ECSA loss rate. This result is also in line with

the observations in [12,29,52,53]. Consequently, model parameters, $k_{dis} \cdot c_p^{ref}$ and k_{rdp} are most sensitive to the following AST properties: UPL, hold time and temperature. Only a slight dependency on RH is expected and the LPL should also have only a minor influence. The related empirical trends are part of the model formulation (see Eqs. (11) and (12)). Fig. 3a shows cathode half cell voltages during aging for an exemplary data set obtained with AST 1. The half cell voltage (Fig. 3a) is plotted logarithmically with respect to current density, to better focus the Tafel slopes. Evidently, the linear slope in the current density range between 0.0 and ~1.2 A/cm^2 seems constant on first sight as cycling progresses. But if analyzed in detail, (see Fig. 3b blue dashes) the Tafel slope is increasing from initial 65 mV/dec to 85 mV/dec at the end of test. At the same time, the exchange current density extracted from the range 0.0 0.2 A/cm^2 goes through a maximum (Fig. 3b orange dotted). Simultaneously, the particle radius distribution is shifted to bigger particles and the ECSA is reduced (Fig. 3b black solid). The observed changes of the activity parame ters might be linked to dealloying, or changes in the distribution of the crystal facets. While dealloying reduces the activity enhancing strain and ligand effects [23,81,82], might impact due to altered relevance of differing reaction pathways. We hypothesize that the surface of the most active facet (111) at low current density (~120 mV/dec [83]) might degrade less or even grows at the cost of the most active facet (110) at high current density (~60 mV/dec [83]) [84], as this facet is most prone to degradation [85]. The increasing m and i$_0$ in this study would be a consequence of fitting these overlapping kinetics in the specific current density window. Coming back to the higher current densities in Fig. 3a, the curves are bending down, the earlier the larger the number of AST cycles. These high current Tafel slopes are much steeper compared to the ones obtained for lower current densities and found frequently in literature [10,13,15,28,34]. A variety of reasons for this behavior is given, like an increased mass transport [10,13], a reduced proton conductivity due to leaching of alloy ions into the ionomer phase [28], catalyst poisoning due to a adsorbing ionomer [86, 87] changed reaction kinetics mechanism [31,88]. In our opinion, an unambiguous answer to this phenomena is still missing [10]. However, in this study this is of secondary importance as the operation range of heavy duty vehicles is focused on lower current densities.

In Fig. 3c, the kinetic voltage losses are presented alongside with the corresponding kinetic voltage loss simulation. After 500 AST cycles, the calculated aging related cathode voltage losses are more or less con stant over the analyzed current range. With progressing AST cycling, this behavior changes and the losses show a wave like behavior: The additional losses in cathode potential increase up to a current range between 0.2 and 0.6 A/cm^2 depending on the number of AST cycles. For higher current densities, in a medium range (0.3 1.4 A/cm^2), a de crease of the kinetic voltage losses can be observed, more pronounced for 15,500, 31,500 and 63,500 AST cycles, compared to 500, 1500 and 3500 AST cycles. For even higher current densities the voltage losses increase again, rapidly.
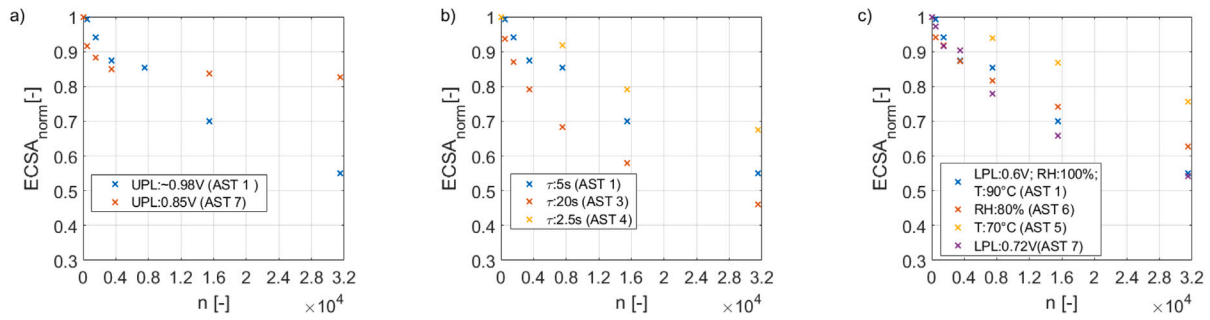
Fig. 2. Measured ECSA evolution depending on the AST conditions UPL, hold time and T,RH, LPL and the number of AST cycles. As reference the data measured for AST 1 represented by the blue data points in the Figs. a–c are used. (a) Influence of the UPL variation on the ECSA decay; (b) Influence of the hold time τ at the UPL and LPL in the ECSA decay; (c) Influence of RH,T and LPL variation on the ECSA decay. (For interpretation of the references to color in this figure legend, the reader is referred to the web version of this article.)
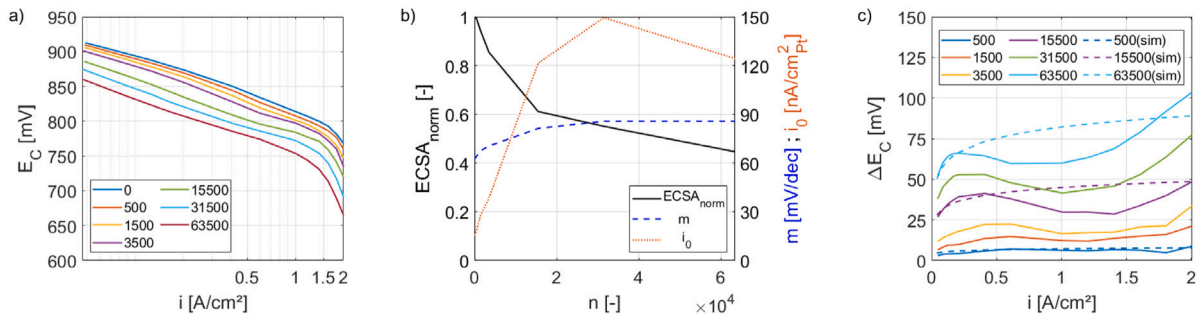
Fig. 3. Exemplary data set obtained within the degradation process of AST 1 (see Table 1) a) Half cell voltage of the cathode; (b) Measured evolution of ECSA, m and i_0 depending on the number of AST cycles n; (c) Determined voltage losses (solid lines) using the calculated half cell voltages shown in (a) and simulated voltage losses (dashed lines) for n: 500, 15,500 and 63,500 .

The increase of cathode voltage loss for small current densities can be related to the increase of the kinetic overpotential with ongoing degradation [15,21,24] in line with the model presented in this paper. Contrary, to this increase, the voltage losses decreases in the medium range of the current density. This observation can be related to a changed oxide formation on the active sites of the PtCo catalyst: For highly degraded MEAs, the half cell voltage for current densities be tween 0.6 and 1.2 A/cm^2 falls below $\sim$ 820 mV. Below this voltage, the influence of surface oxides on the obtained cell voltage is significantly reduced (10 30 mV) as shown in Fig. 5 in [9]. These benefits from reduced oxide loadings after Pt dissolution testing is not part of our model. Accordingly, the benefits in the medium current range cannot be predicted. The rapid increase of the performance losses at even high current densities above 1.2 A/cm^2 is in line with observations made by [10,13,15,28,34] but also not part of our model. This increase can be related to the change of Tafel slope at high current densities discussed earlier, whose origin is yet to be identified unambiguously.

4.2. Evaluation of the ECSA loss model

Fig. 4a compares the simulated data with ECSA results obtained from the AST experiments. It can be seen that the mechanistic based model presented in Section 3.1 complies with the experimental data gathered with a variety of aging conditions. With a standard devi ation of 1.52%, the model shows a good accuracy compared to the experimental data.

This result shows, that the model presented in Section 3.1 can be used to describe $ECSA$ losses under different operation conditions, by assuming dissolution and redeposition of the catalyst as governing degradation mechanism.

Table 3
Overview of the parameters used in the empirical correlations (see equations (15) and (16)).

Parameter	Value	Unit
p_1	39.59	[mV/dec]
p_2	−101.19	[mV/dec]
p_3	$735.13 \cdot 10^{-9}$	[A/cm$^2_{Pt}$]
p_4	−3.9049	[–]

4.3. Correlating tafel slope and exchange current density with ECSA

Fig. 5 shows the experimentally determined $m(n)$ and $i_0(n)$ vs. the normalized ECSA values obtained with the different ASTs (see Table 1). In order to reduce the influence of the measurement noise and to avoid an overestimation of data points measured at high degradation rates, the measured data are averaged within $ECSA_{norm}$ steps of 10%. The resulting standard deviations are shown with the vertical and horizontal bars in Fig. 5.

The potential mechanisms behind these trends were discussed ear lier (see Section 4.1). It can be seen that the Tafel slope correlates linearly with ECSA$_{norm}$, while the exchange current density shows an exponential dependency,

$$m(ECSA_{norm}) = p_1 \cdot ECSA_{norm} + p_2 \tag{15}$$

and

$$i_0(ECSA_{norm}) = p_3 \cdot e^{(p_4 \cdot ECSA_{norm})}, \tag{16}$$

with the parameters given in Table 3.

4.4. Evaluation of the kinetic voltage loss model

In Fig. 6a, the accuracy of the kinetic voltage loss model is demon strated by comparing simulated and experimental kinetic voltage losses
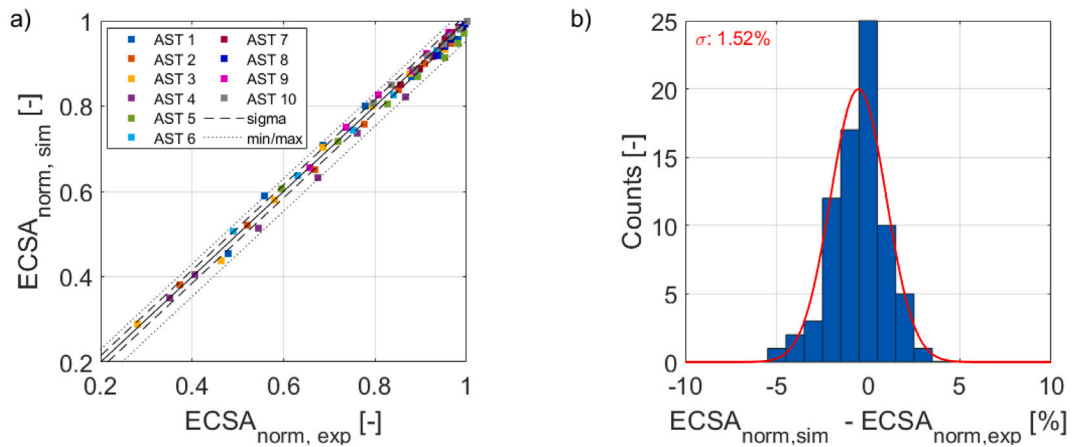
Fig. 4. (a) Comparison of the simulated and experimentally obtained electrochemical active surface area development within the accelerated stress tests. (b) Histogram of the simulated and experimentally obtained electrochemical active surface area development within the accelerated stress tests.
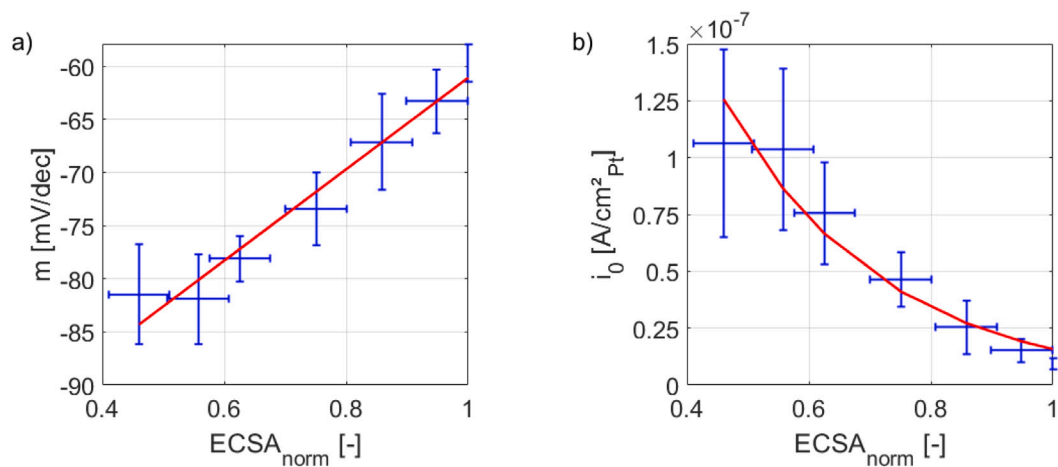
Fig. 5. (a) Correlation between averaged Tafel slopes and the normalized ECSA. The empirical correlation is based on a linear equation (red line). (b) Correlation between averaged exchange current densities and the normalized ECSA. The empirical correlation is based on a exponential function (red line). (For interpretation of the references to color in this figure legend, the reader is referred to the web version of this article.)

in the range of 0.0 1.2 A/cm^2 (low and medium current range). The histogram shown in Fig. 6b analyzes the accuracy of the model, by presenting the difference between simulation and experiment on the x axis and the counts of these differences on the y axis. With a standard deviation of 5.3 mV the model describes the kinetic voltage losses in PEM FCs with a good accuracy.

The model shows some inaccuracies especially at high kinetic volt age losses, which are related to high degrees of degradation. We relate this to a changed oxide formation on the active sites of the PtCo catalyst [9], as discussed in Section 4.1. These findings can also be seen by comparing the simulated performance losses with the measured performance losses in Fig. 3c. It can be seen, that the voltage losses in current density range between 0.0 and ~0.4 A/cm^2 are almost perfectly described with the model, independently from the number of AST cycles. In the medium current range (0.4 1.2 A/cm^2, represented by the green data points), the model overestimates the voltage losses, as it does not account for the changed influence of PtOx.

To get an impression whether the model is also valid over a wider range of performance, the model is analyzed for a current density range from 0.0 up to 2.0 A/cm^2. The result is shown in Fig. 7. It can be seen that the maximal overestimation of the performance losses in Fig. 7 (max: 29.2 mV) is identical to the values in Fig. 6, showing that the related test points are already part of the smaller data set. For the un derestimation of the voltage losses a slight increase from −10.3 mV up to 12.9 mV is obtained. Furthermore, the standard deviation increases

by about 34% from 5.3 mV to 7.1 mV. This broadening of the standard deviation is on the one hand related to a significantly increased num ber of data points with overestimated performance losses, at current densities between 1.2 and 1.8 A/cm^2. Especially these load points are also impacted by the changed oxide formation (shown with the cyan data points in Fig. 7a). On the other hand the model shows a higher inaccuracy at 2.0 A/cm^2 (represented with the orange data points in Fig. 7a). At these high current densities and high degrees of degradation the change in high current Tafel slope plays a major role (see also Fig. 3 a and c) and the model starts to systematically underpredict the related losses. Hence, if the model was to be applied to high current densities, e.g. in LDV, it requires an additional contribution, probably linked to the high current Tafel slope.

4.5. Deciphering the kinetic voltage loss model

We finalize the discussion by first breaking down the total loss $\Delta E_C(n)$ into contributions arising from changes in ECSA as well as changes in m and i$_0$. While the former represents the impact of chang ing catalyst surface area, the later show the relevance of a changed ac tivity parameters (as discussed in Section 4.1). Afterwards, we analyze the relevance of these contributions. The performance loss $\Delta E_C(n, i)$ can be split into three contributions (shown in the supplementary material C)

$$\Delta E_C(n, i) = \Delta\eta_{ORR,m}(n, i) + \Delta\eta_{ORR,m,i0}(n) + \Delta\eta_{ORR,m\,ECSA}(n), \qquad (17)$$
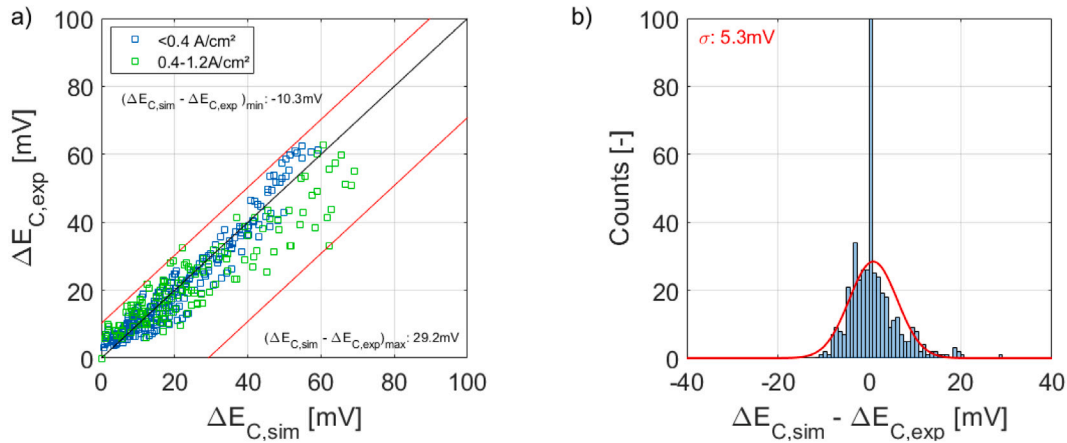
Fig. 6. (a) Comparison of the simulated and experimentally obtained degradation related performance losses in a current density range of 0.0–1.2 A/cm^2. The black lines represents the parity line and the red lines mark the maximum under — respectively overestimation of the measured voltages losses by the model; (b) Histogram of the simulated and experimentally obtained voltage losses in a range of 0–1.2 A/cm^2 with a standard deviation σ of 5.3 mV. (For interpretation of the references to color in this figure legend, the reader is referred to the web version of this article.)
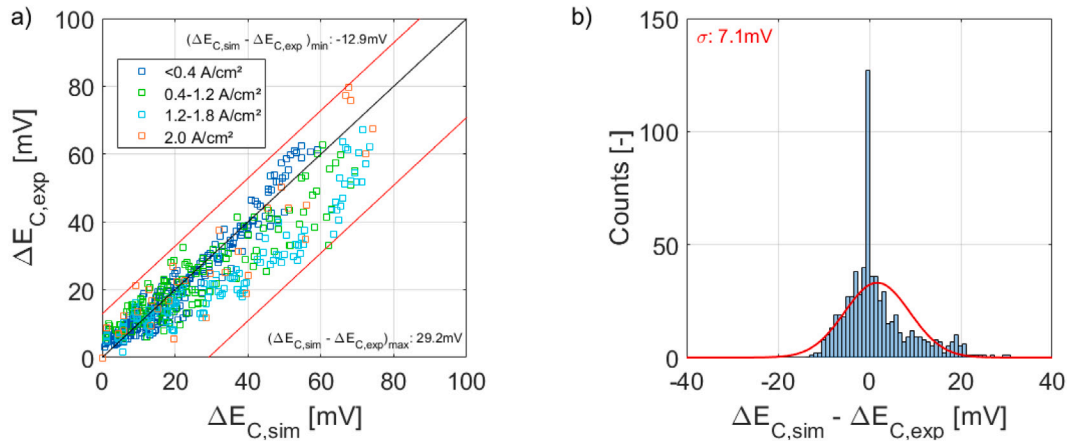
Fig. 7. (a) Comparison of the simulated and experimentally obtained degradation related performance losses in a current density range of 0.0–2.0 A/cm^2. The black lines represents the parity line and the red lines mark the maximum under — respectively overestimation of the measured voltages losses by the model; (b) Histogram of the simulated and experimentally obtained voltage losses in a range of 0–2.0 A/cm^2 with a standard deviation σ of 7.1 mV. (For interpretation of the references to color in this figure legend, the reader is referred to the web version of this article.)

with the first contribution representing the overpotential change caused by a change of Tafel slope $m(n)$

$$\Delta\eta_{ORR,m}(n,i) = (m(n) - m(0)) \cdot log\left(\frac{i}{i_0(0) \cdot ECSA(0)}\right). \tag{18}$$

The second contributor describes the combined influence of $m(n)$ and $i_0(n)$ on the overpotential

$$\Delta\eta_{ORR,m,i0}(n) = m(n) \cdot log\left(\frac{i_0(0)}{i_0(n)}\right)$$

$$= \underbrace{m(0) \cdot log\left(\frac{i_0(0)}{i_0(n)}\right)}_{\Delta\eta_{ORR,m,i0,1}(n)} + \underbrace{(m(n) - m(0)) \cdot log\left(\frac{i_0(0)}{i_0(n)}\right)}_{\Delta\eta_{ORR,m,i0,2}(n)}. \tag{19}$$

The third contributor combines the overpotential change due to re duced $ECSA(n)$ and the influence of $m(n)$

$$\Delta\eta_{ORR,m,ECSA}(n)$$

$$= m(n) \cdot log\left(\frac{ECSA(0)}{ECSA(n)}\right)$$

$$= \underbrace{m(0) \cdot log\left(\frac{ECSA(0)}{ECSA(n)}\right)}_{\Delta\eta_{ORR,m,ECSA,1}(n)} + \underbrace{(m(n) - m(0)) \cdot log\left(\frac{ECSA(0)}{ECSA(n)}\right)}_{\Delta\eta_{ORR,m,ECSA,2}(n)}. \tag{20}$$

Thereby, the differentiation into two terms indexed with "1" and "2" in Eq. (19) is meaningfull as the two terms represent i_0 linked voltage loss contributions referred to the Tafel slope begin of life and the change of Tafel slope over the course of testing, respectively. The same applies to the ESCA losses in Eq. (20). Below, we will show that the terms with "2" can be neglected. Accordingly, the voltage loss contributions from change of Tafel slope, exchange current density and ECSA can be separated. Figs. 8a, b, and c represent this deconvolution for simulated performance losses caused by the operating conditions of AST 1 after 500, 15,500 and 63,500 AST cycles. To get an impression of how $\Delta\eta_{ORR,m}$ is influenced by the current density, the deconvolution is shown at 0.04, 0.2, 0.6, 1.0 and 1.8 A/cm^2. Positive values are voltage losses, which are obtained for $\Delta\eta_{ORR,m}$ and $\Delta\eta_{ORR,m,ECSA,1}$ and $\Delta\eta_{ORR,m,ECSA,2}$. Negative values can be interpreted as voltage "gains" due to a increasing i_0 (see Fig. 1b resulting in negative values for $\Delta\eta_{ORR,m,i_0,1}$ and $\Delta\eta_{ORR,m,i_0,2}$. Generally, it can be seen that the secondary contributions $\Delta\eta_{ORR,m,i_0,2}$ and $\Delta\eta_{ORR,m,ECSA,2}$ are of minor importance and can be neglected. Consequently, the evaluation of ΔE_C can be done by analyzing $\Delta\eta_{ORR,m,ECSA1}$ related to a reduced ECSA and the sum of "$\Delta\eta_{ORR,m}+\Delta\eta_{ORR,m,i_0,1}$", representing the impact of deallyoing or altered facet distribution. It can be seen that the voltage losses are dominated by $\Delta\eta_{ORR,m}+\Delta\eta_{ORR,m,i_0,1}$, which cause at least 50% of the voltage losses. These losses are higher than the losses caused by losses of ECSA. This
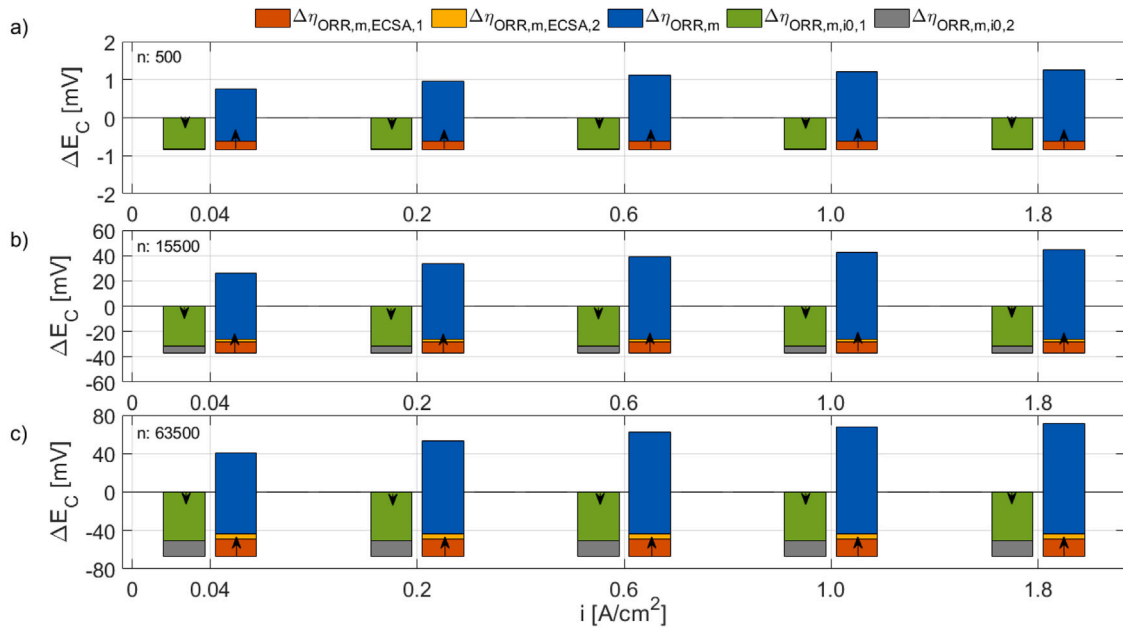
Fig. 8. Deconvolution of kinetic voltage losses simulated with the introduced model with the operating conditions of AST 1 after: (a) 500 AST cycles, representing a low level of degradation; (b) 15,500 AST cycles, representing a mid level of degradation and (c) 63,500 AST cycles, representing a high level of degradation cycles.

conclusion is the same, no matter which AST or which cycle number is considered. Accordingly, Fig. 8 reveals that the poorly understood con tributor to End of Life performance losses, namely change of activity, is of major importance, while well understood losses associated with catalyst surface changes are of much lower importance.

5. Conclusion

In this work, a model for the degradation of alloy catalysts in polymer electrolyte membrane fuel cells is developed. The model con sists of two submodels, the first submodel accounts for the changes in electrochemically active surface, the second submodel accounts for changes in the activity of the catalyst material, probably caused by dealloying and changes in the distribution of crystal facets.

The changes in electrochemically active surface were modeled with a statistical physics based model that describes the evolution of the particle radius distribution based on particle altering processes, includ ing dissolution and redeposition. This model was fitted to ECSA data obtained within accelerated stress tests, which were performed over a wide range of operating conditions. The obtained model parameters, i.e. dissolution and redeposition rate constants, were described as func tions of the AST operating conditions using empirical relationships to parameterize these dependencies. With this semi empirical ECSA loss model, the experimentally determined ECSA losses were reproduced with a standard deviation of 1.52% in a range of 0 50% total surface loss.

The second submodel is based on a generalized Tafel approach. It is coupled to the first submodel by using experimentally found cor relations between ECSA and the Tafel parameters, namely Tafel slope and exchange current density. After parametrization, degradation was predicted for ASTs of a wide parameter range for a current range of 0.0 2.0 A/cm^2 with a standard deviation of 7.1 mV. By reducing the current density range to 0.0 1.2 A/cm^2, the accuracy of the model improves to 5.3 mV. Systematic deviations are in our opinion a consequence of the voltage loss model's simplicity. As reduced oxide loadings in a current density range between 0.6 and 1.2 A/cm^2 for degraded cathodes are ignored, the model overestimates the losses in this range. Oppositely, at higher current densities, the kinetic voltage losses are underestimated as the model disregards the possibility of a changing Tafel slope. Despite these limitations, the presented model allows to interpret the

kinetic voltage loss as a sum of overpotentials related to a loss of electrochemical surface area and changes of the activity. Interestingly, we find that the performance losses for the MEA used in this work are not described sufficiently due to loss of electrochemical active surface area alone, as at least 50% of the voltage losses are caused by the overpotentials related explicitly to a changing activity parameters. Accordingly, this study shows that during cathode degradation studies of PEM FCs, Tafel slope and exchange current density should be the most relevant metric, not the electrochemical surface area.

Abbreviations

Accelerated Stress Test	AST
Begin of Life	BoL
Cyclic Voltammetry	CV
Department of Energy	DoE
Electrochemical active surface area	ECSA
End of Test	EoT
Electrochemical Impedance Spectroscopy	EIS
High Frequency Resistance	HFR
Lower Potential Limit	LPL
Membrane Electrode Assembly	MEA
Open Circuit Voltage	OCV
Oxygen Reduction Reaction	ORR
Particle Radius Distribution	PRD
Platinum Oxide	PtOx
Proton Exchange Membrane Fuel Cell	PEM FC
Upper Potential Limit	UPL

List of Symbols

Symbol	Description	Unit
A	Active area of the MEA	[cm^2]
$c_{Pt}^-(t)$	Averaged Pt concentration	[mol m^{-3}]
c_{Pt}^{ref}	Reference Pt concentration	[mol m^{-3}]
E_C	Cathode overpotential	[V]
$ECSA$	Electrochemical active surface area	[cm$_{Pt}^2$ cm^{-2}]
$ECSA_{norm}$	Normalized electrochemical active surface area	[ ]

F	Faraday constant	$[\mathrm{Cmol^{-1}}]$
f_N	Dimensionless normalized particle radius distribution function	$[\ ]$
g_τ	Correlation factor k_{dis} τ	$[\mathrm{s^{-1}}]$
g_{LPL}	Correlation factor k_{dis} LPL	$[\mathrm{V^{-1}}]$
g_{UPL}	Correlation factor k_{dis} UPL	$[\mathrm{V^{-1}}]$
g_{RH}	Correlation factor k_{dis} RH	$[\ ]$
g_T	Correlation factor k_{dis} T	$[\mathrm{K^{-1}}]$
h_τ	Correlation factor k_{rdp} τ	$[\mathrm{s^{-1}}$
h_{UPL}	Correlation factor k_{rdp} UPL	$[\mathrm{V^{-1}}]$
i	Current density	$[\mathrm{Acm^{-2}}]$
i_0	Exchange current density	$[\mathrm{Acm_{Pt}^{-2}}]$
J^-	Extinction term in the Smoluchowski coagulation equation	$[\mathrm{s^{-1}}]$
J^+	Creation term in the Smoluchowski coagulation equation	$[\mathrm{s^{-1}}]$
k_{det}	Detachment rate	$[\mathrm{s^{-1}}]$
k_{rdp}	Redeposition rate	$[\mathrm{ms^{-1}}]$
k_{dis}	Dissolution rate	$[\mathrm{ms^{-1}}]$
k_{det}	Detachment rate	$[\mathrm{s^{-1}}]$
m_V	Pt mass loading per unit volume	$[\mathrm{gm^{-3}}]$
M_{Pt}	Molecular weight of Pt	$[\mathrm{gmol^{-1}}]$
$M_N(t)$	Normalized dimensionless mass moment of fN (r,t)	$[\ ]$
m	Tafel slope	$[\mathrm{mVdec^{-1}}]$
n	Number of AST cycles	$[\ ]$
p_1	Empirical correlation parameter	$[\mathrm{mVdec^{-1}}]$
p_2	Empirical correlation parameter	$[\mathrm{mVdec^{-1}}]$
p_3	Empirical correlation parameter	$[\mathrm{Acm_{Pt}^{-2}}]$
p_4	Empirical correlation parameter	$[\ ]$
p_{O2}	Oxygen partial pressure	$[\mathrm{Pa}]$
R_0	Characteristic particle radius	$[\mathrm{nm}]$
r	Particle radius	$[\mathrm{nm}]$
R	Ideal gas constant	$[\mathrm{Jmol^{-1}K^{-1}}]$
R_{HFR}	High frequency resistance	$[\mathrm{m\Omega}]$
R_{mt}	Oxygen mass transport resistance	$[\mathrm{scm^{-1}}]$
R_{H^+}	Proton transport resistance	$[\mathrm{m\Omega}]$
T	Temperature	$[\mathrm{K}]$
U_{Cell}	Measured cell voltage	$[\mathrm{mV}]$
V_m	Molar volume of Pt	$[\mathrm{m^3mol^{-1}}]$

Greek Symbols

Symbol	Description	Unit
α	Transfer coefficient	$[\ ]$
γ	ORR reaction order wrt. to p_{O_2}	$[\ ]$
η_{H^+}	Overpotential related to proton transport through the ionomer	$[\mathrm{mV}]$
η_{HFR}	Overpotential related to Ohmic resistance	$[\mathrm{mV}]$
η_{ORR}	Overpotential related to the ORR	$[\mathrm{mV}]$
η_{mt}	Overpotential related to oxygen mass transport	$[\mathrm{mV}]$
τ	Hold time in an accelerated stress	$[\mathrm{s}]$
τ_{ref}	Hold time of the reference accelerated stress	$[\mathrm{s}]$

CRediT authorship contribution statement

David Bernhard: Conceptualization, Writing – original draft, Methodology, Data curation, Investigation, Visualization, Software. **Thomas Kadyk:** Conceptualization, Methodology, Writing – review & editing, Software. **Sebastian Kirsch:** Conceptualization, Methodology, Writing – review & editing, Software. **Hannes Scholz:** Methodology, Writing – review & editing, Software. **Ulrike Krewer:** Supervision, Writing – review & editing.

Declaration of competing interest

The authors declare that they have no known competing financial interests or personal relationships that could have appeared to influence the work reported in this paper.

Data availability

The authors do not have permission to share data.

Appendix A. Supplementary data

Supplementary material related to this article can be found online at https://doi.org/10.1016/j.jpowsour.2023.232771.

References

[1] H. Wang, R. Wang, S. Sui, T. Sun, Y. Yan, S. Du, Cathode design for proton exchange membrane fuel cells in automotive applications, Autom. Innov. 4 (2) (2021) 144–164.

[2] A. Lozanovski, N. Whitehouse, N. Ko, S. Whitehouse, Sustainability assessment of fuel cell buses in public transport, Sustainability 10 (5) (2018) 1480.

[3] D.A. Cullen, K.C. Neyerlin, R.K. Ahluwalia, R. Mukundan, K.L. More, R.L. Borup, A.Z. Weber, D.J. Myers, A. Kusoglu, New roads and challenges for fuel cells in heavy-duty transportation, Nat. Energy 6 (5) (2021) 462–474.

[4] H. Yu, M.J. Zachman, C. Li, L. Hu, N.N. Kariuki, R. Mukundan, J. Xie, K.C. Neyerlin, D.J. Myers, D.A. Cullen, Recreating fuel cell catalyst degradation in aqueous environments for identical-location scanning transmission electron microscopy studies, ACS Appl. Mater. Interfaces 14 (18) (2022) 20418–20429.

[5] Y. Wang, D.F. Ruiz Diaz, K.S. Chen, Z. Wang, X.C. Adroher, Materials, technological status, and fundamentals of PEM fuel cells – a review, Mater. Today 32 (2020) 178–203.

[6] C.S. Gittleman, H. Jia, E.S. de Castro, C.R. Chisholm, Y.S. Kim, Proton conductors for heavy-duty vehicle fuel cells, Joule 5 (7) (2021) 1660–1677.

[7] Y. Wang, Y. Pang, H. Xu, A. Martinez, K.S. Chen, PEM Fuel cell and electrolysis cell technologies and hydrogen infrastructure development – a review, Energy Environ. Sci. 15 (6) (2022) 2288–2328.

[8] M. Messing, E. Kjeang, Empirical modeling of cathode electrode durability in polymer electrolyte fuel cells, J. Power Sources 451 (2020) 227750.

[9] D. Bernhard, T. Kadyk, U. Krewer, S. Kirsch, How platinum oxide affects the degradation analysis of PEM fuel cell cathodes, Int. J. Hydrogen Energy 46 (26) (2021) 13791–13805.

[10] G.S. Harzer, J.N. Schwämmlein, A.M. Damjanović, S. Ghosh, H.A. Gasteiger, Cathode loading impact on voltage cycling induced PEMFC degradation: A voltage loss analysis, J. Electrochem. Soc. 165 (6) (2018) F3118–F3131.

[11] T. Jahnke, G.A. Futter, A. Baricci, C. Rabissi, A. Casalegno, Physical modeling of catalyst degradation in low temperature fuel cells: Platinum oxidation, dissolution, particle growth and platinum band formation, J. Electrochem. Soc. 167 (1) (2019) 013523.

[12] P. Schneider, C. Sadeler, A.-C. Scherzer, N. Zamel, D. Gerteisen, Fast and reliable state-of-health model of a PEM cathode catalyst layer, J. Electrochem. Soc. 166 (4) (2019) F322–F333.

[13] A. Kneer, N. Wagner, A semi-empirical catalyst degradation model based on voltage cycling under automotive operating conditions in PEM fuel cells, J. Electrochem. Soc. 166 (2) (2019) F120–F127.

[14] A.A. Topalov, S. Cherevko, A.R. Zeradjanin, J.C. Meier, I. Katsounaros, K.J.J. Mayrhofer, Towards a comprehensive understanding of platinum dissolution in acidic media, Chem. Sci. 5 (2) (2014) 631–638.

[15] P. Zihrul, I. Hartung, S. Kirsch, G. Huebner, F. Hasché, H.A. Gasteiger, Voltage cycling induced losses in electrochemically Active Surface Area and in H2/air-performance of PEM fuel cells // voltage cycling induced losses in electrochemically Active Surface Area and in H 2 /air-performance of PEM fuel cells, J. Electrochem. Soc. 163 (6) (2016) F492–F498.

[16] H. Zhang, H. Haas, J. Hu, S. Kundu, M. Davis, C. Chuy, The impact of potential cycling on PEMFC durability, J. Electrochem. Soc. 160 (8) (2013) F840–F847.

[17] F.A. de Bruijn, V.A.T. Dam, G.J.M. Janssen, Review: Durability and degradation issues of PEM fuel cell components, Fuel Cells 8 (1) (2008) 3–22.

[18] J.C. Meier, Degradation phenomena and design principles for stable and active Pt/C fuel cell catalysts, 2013.

[19] N. Yousfi-Steiner, P. Moçotéguy, D. Candusso, D. Hissel, A review on polymer electrolyte membrane fuel cell catalyst degradation and starvation issues: Causes, consequences and diagnostic for mitigation, J. Power Sources 194 (1) (2009) 130–145.

[20] S. Zhang, X.-Z. Yuan, J.N.C. Hin, H. Wang, K.A. Friedrich, M. Schulze, A review of platinum-based catalyst layer degradation in proton exchange membrane fuel cells, J. Power Sources 194 (2) (2009) 588–600.

[21] S. Arisetty, X. Wang, R.K. Ahluwalia, R. Mukundan, R. Borup, J. Davey, D. Langlois, F. Gambini, O. Polevaya, S. Blanchet, Catalyst durability in PEM fuel cells with low platinum loading, J. Electrochem. Soc. 159 (5) (2012) B455–B462.

[22] L. Dubau, F. Maillard, M. Chatenet, J. André, E. Rossinot, Nanoscale compositional changes and modification of the surface reactivity of Pt3Co/C nanoparticles during proton-exchange membrane fuel cell operation, Electrochim. Acta 56 (2) (2010) 776–783.

[23] F. Jiang, F. Zhu, F. Yang, X. Yan, A. Wu, L. Luo, X. Li, J. Zhang, Comparative investigation on the activity degradation mechanism of Pt/C and PtCo/C electrocatalysts in PEMFCs during the accelerate degradation process characterized by an in situ X-ray absorption fine structure, ACS Catal. 10 (1) (2019) 604–612.

[24] D.D. Papadias, R.K. Ahluwalia, N. Kariuki, D. Myers, R. Borup, D.A. Cullen, B.T. Sneed, K.C. Neyerlin, R. Mukundan, R.L. Borup, Durability of Pt-Co alloy polymer electrolyte fuel cell cathode catalysts under accelerated stress tests, J. Electrochem. Soc. 165 (6) (2018) F3166–F3177.

[25] J. Hou, M. Yang, C. Ke, G. Wei, C. Priest, Z. Qiao, G. Wu, J. Zhang, Platinum-group-metal catalysts for proton exchange membrane fuel cells: From catalyst design to electrode structure optimization, EnergyChem 2 (1) (2020) 100023.

[26] N. Macauley, R. Mukundan, D.A. Langlois, K.C. Neyerlin, S.S. Kocha, K.L. More, M. Odgaard, R.L. Borup, Durability of PtCo/C cathode catalyst layers subjected to accelerated stress testing, ECS Trans. 75 (14) (2016) 281–287.

[27] L.J. Moriau, A. Hrnjić, A. Pavlišič, A.R. Kamšek, U. Petek, F. Ruiz-Zepeda, M. Šala, L. Pavko, V.S. Šelih, M. Bele, P. Jovanovič, M. Gatalo, N. Hodnik, Resolving the nanoparticles' structure-property relationships at the atomic level: a study of Pt-based electrocatalysts, IScience 24 (2) (2021) 102102.

[28] N. Ramaswamy, S. Kumaraguru, W. Gu, R.S. Kukreja, K. Yu, D. Groom, P. Ferreira, High-current density durability of Pt/C and PtCo/C catalysts at similar particle sizes in PEMFCs, J. Electrochem. Soc. 168 (2) (2021) 024519.

[29] N. Ramaswamy, S. Kumaraguru, R.S. Kukreja, D. Groom, K. Jarvis, P. Ferreira, Mitigation of PtCo/C cathode catalyst degradation via control of relative humidity, J. Electrochem. Soc. 168 (12) (2021) 124512.

[30] C. Zalitis, A. Kucernak, X. Lin, J. Sharman, Electrochemical measurement of intrinsic oxygen reduction reaction activity at high current densities as a function of particle size for Pt 4– x Co x /C (x=0, 1, 3) catalysts, ACS Catal. (2020) 4361–4376.

[31] T. Shinagawa, A.T. Garcia-Esparza, K. Takanabe, Insight on Tafel slopes from a microkinetic analysis of aqueous electrocatalysis for energy conversion, Scientific Reports 5 (2015) 13801.

[32] K.C. Neyerlin, W. Gu, J. Jorne, H.A. Gasteiger, Determination of catalyst unique parameters for the oxygen reduction reaction in a PEMFC, J. Electrochem. Soc. 153 (10) (2006) A1955.

[33] S. Komini Babu, R. Mukundan, C. Wang, D. Langlois, D.A. Cullen, D. Papadias, K.L. More, R. Ahluwalia, J. Waldecker, R. Borup, Effect of catalyst and catalyst layer composition on catalyst support durability, J. Electrochem. Soc. 168 (4) (2021) 044502.

[34] J.N. Schwämmlein, G.S. Harzer, P. Pfändner, A. Blankenship, H.A. El-Sayed, H.A. Gasteiger, Activity and stability of carbon supported Pt x Y Alloys for the ORR determined by RDE and single-cell PEMFC measurements, J. Electrochem. Soc. 165 (15) (2018) J3173–J3185.

[35] W. Bi, Q. Sun, Y. Deng, T.F. Fuller, The effect of humidity and oxygen partial pressure on degradation of Pt/C catalyst in PEM fuel cell, Electrochim. Acta 54 (6) (2009) 1826–1833.

[36] K. Benaggoune, M. Yue, S. Jemei, N. Zerhouni, A data-driven method for multi-step-ahead prediction and long-term prognostics of proton exchange membrane fuel cell, Appl. Energy 313 (2022) 118835.

[37] K. Chen, S. Laghrouche, A. Djerdir, Degradation model of proton exchange membrane fuel cell based on a novel hybrid method, Appl. Energy 252 (2019) 113439.

[38] J. Fu, Z. Fu, S. Song, Proton membrane fuel cell stack performance prediction through deep learning method, Energy Rep. 8 (2022) 5387–5395.

[39] E. Maleki, N. Maleki, Artificial neural network modeling of Pt/C cathode degradation in PEM fuel cells, J. Electron. Mater. 45 (8) (2016) 3822–3834.

[40] H. Zhen, W. Gong, L. Wang, Offline data–driven evolutionary optimization based on model selection, Swarm Evol. Comput. 71 (2022) 101080.

[41] A. Tang, Y. Yang, Q. Yu, Z. Zhang, L. Yang, A review of life prediction methods for PEMFCs in electric vehicles, Sustainability 14 (16) (2022) 9842.

[42] R.-H. Lin, X.-N. Xi, P.-N. Wang, B.-D. Wu, S.-M. Tian, Review on hydrogen fuel cell condition monitoring and prediction methods, Int. J. Hydrogen Energy 44 (11) (2019) 5488–5498.

[43] J. Zhao, X. Li, C. Shum, J. McPhee, A review of physics-based and data-driven models for real-time control of polymer electrolyte membrane fuel cells, Energy AI 6 (2021) 100114.

[44] J. Kim, M. Kim, T. Kang, Y.-J. Sohn, T. Song, K.H. Choi, Degradation modeling and operational optimization for improving the lifetime of high-temperature PEM (proton exchange membrane) fuel cells, Energy 66 (2014) 41–49.

[45] H. Chen, P. Pei, M. Song, Lifetime prediction and the economic lifetime of Proton Exchange Membrane fuel cells, Appl. Energy 142 (2015) 154–163.

[46] X. Zhang, D. Yang, M. Luo, Z. Dong, Load profile based empirical model for the lifetime prediction of an automotive PEM fuel cell, Int. J. Hydrogen Energy 42 (16) (2017) 11868–11878.

[47] T.-W. Lee, A.A. Tseng, K.-S. Bae, Y.H. Do, Simulation of the proton-exchange membrane (PEM) fuel cell life-cycle performance with data-driven parameter estimation, Energy Fuels 24 (3) (2010) 1882–1888.

[48] P. Pei, Q. Chang, T. Tang, A quick evaluating method for automotive fuel cell lifetime, Int. J. Hydrogen Energy 33 (14) (2008) 3829–3836.

[49] M.K. Debe, A.K. Schmoeckel, G.D. Vernstrom, R. Atanasoski, High voltage stability of nanostructured thin film catalysts for PEM fuel cells, J. Power Sources 161 (2) (2006) 1002–1011.

[50] W. Bi, T.F. Fuller, Temperature effects on PEM fuel cells Pt-C catalyst degradation, J. Electrochem. Soc. 155 (2008).

[51] S.S. Kocha, Electrochemical degradation, in: Polymer Electrolyte Fuel Cell Degradation, Elsevier, 2012, pp. 89–214.

[52] R.K. Ahluwalia, S. Arisetty, J.-K. Peng, R. Subbaraman, X. Wang, N. Kariuki, D.J. Myers, R. Mukundan, R. Borup, O. Polevaya, Dynamics of particle growth and Electrochemical Surface Area loss due to platinum dissolution, J. Electrochem. Soc. 161 (3) (2013 // 2014) F291–F304.

[53] W. Bi, Q. Sun, Y. Deng, T.F. Fuller, The effect of humidity and oxygen partial pressure on degradation of Pt-C catalyst in PEM fuel cell, Electrochim. Acta 54 (2009) 1826–1833.

[54] E.F. Holby, D. Morgan, Application of Pt nanoparticle dissolution and oxidation modeling to understanding degradation in PEM fuel cells, J. Electrochem. Soc. 159 (5) (2012) B578–B591.

[55] P. Urchaga, T. Kadyk, S.G. Rinaldo, A.O. Pistono, J. Hu, W. Lee, C. Richards, M.H. Eikerling, C.A. Rice, Catalyst degradation in fuel cell electrodes // catalyst degradation in fuel cell electrodes: Accelerated stress tests and model-based analysis: Accelerated stress tests and model-based analysis, Electrochim. Acta 176 (2015) 1500–1510.

[56] T. Jahnke, G. Futter, A. Latz, T. Malkow, G. Papakonstantinou, G. Tsotridis, P. Schott, M. Gérard, M. Quinaud, M. Quiroga, A.A. Franco, K. Malek, F. Calle-Vallejo, R. Ferreira de Morais, T. Kerber, P. Sautet, D. Loffreda, S. Strahl, M. Serra, P. Polverino, C. Pianese, M. Mayur, W.G. Bessler, C. Kompis, Performance and degradation of Proton Exchange Membrane Fuel Cells: State of the art in modeling from atomistic to system scale, J. Power Sources 304 (2016) 207–233.

[57] Y. Li, K. Moriyama, W. Gu, S. Arisetty, C.Y. Wang, A one-dimensional Pt degradation model for polymer electrolyte fuel cells, J. Electrochem. Soc. 162 (8) (2015) F834–F842.

[58] Y. Yang, M. Bai, J. Lv, L. Gao, Y. Li, X. Lv, Y. Li, Y. Song, One-dimensional modeling for aging of Pt-Co core-shell catalysts in proton exchange membrane fuel cells, J. Electrochem. Soc. 169 (5) (2022) 054526.

[59] H.A. Baroody, D.B. Stolar, M.H. Eikerling, Modelling-based data treatment and analytics of catalyst degradation in polymer electrolyte fuel cells, Electrochim. Acta 283 (2018) 1006–1016.

[60] S.G. Rinaldo, P. Urchaga, J. Hu, W. Lee, J. Stumper, C. Rice, M. Eikerling, Theoretical analysis of electrochemical surface-area loss in supported nanoparticle catalysts, Phys. Chem. Chem. Phys. PCCP 16 (48) (2014) 26876–26886.

[61] S.G. Rinaldo, W. Lee, J. Stumper, M. Eikerling, Catalyst degradation: Nanoparticle population dynamics and kinetic processes, ECS Trans. 50 (2) (2013) 1505–1513.

[62] S.G. Rinaldo, W. Lee, J. Stumper, M. Eikerling, Nonmonotonic dynamics in Lifshitz-Slyozov-Wagner theory: Ostwald ripening in nanoparticle catalysts, Phys. Rev. E 86 (4) (2012) 041601.

[63] H.A. Baroody, E. Kjeang, Predicting platinum dissolution and performance degradation under drive cycle operation of polymer electrolyte fuel cells, J. Electrochem. Soc. 168 (4) (2021) 044524.

[64] M. Moein-Jahromi, M.J. Kermani, S. Movahed, Degradation forecast for PEMFC cathode-catalysts under cyclic loads, J. Power Sources 359 (2017) 611–625.

[65] L. Lu, M. Ouyang, H. Huang, P. Pei, F. Yang, A semi-empirical voltage degradation model for a low-pressure proton exchange membrane fuel cell stack under bus city driving cycles, J. Power Sources 164 (1) (2007) 306–314.

[66] J.M. Desantes, R. Novella, B. Pla, M. Lopez-Juarez, A modeling framework for predicting the effect of the operating conditions and component sizing on fuel cell degradation and performance for automotive applications, Appl. Energy 317 (2022) 119137.

[67] M. Ou, R. Zhang, Z. Shao, B. Li, D. Yang, P. Ming, C. Zhang, A novel approach based on semi-empirical model for degradation prediction of fuel cells, J. Power Sources 488 (2021) 229435.

[68] C. Robin, M. Gérard, M. Quinaud, J. d'Arbigny, Y. Bultel, Proton exchange membrane fuel cell model for aging predictions: Simulated equivalent active surface area loss and comparisons with durability tests, J. Power Sources 326 (2016) 417–427.

[69] M. Moein-Jahromi, M.J. Kermani, Performance prediction of PEM fuel cell cathode catalyst layer using agglomerate model, Int. J. Hydrogen Energy 37 (23) (2012) 17954–17966.

[70] D.R. Baker, D.A. Caulk, K.C. Neyerlin, M.W. Murphy, Measurement of oxygen transport resistance in PEM fuel cells by limiting current methods, J. Electrochem. Soc. 156 (9) (2009) B991.

[71] J.P. Owejan, J.E. Owejan, W. Gu, Impact of platinum loading and catalyst layer structure on PEMFC performance, J. Electrochem. Soc. 160 (8) (2013) F824–F833.

[72] R. Makharia, M.F. Mathias, D.R. Baker, Measurement of catalyst layer electrolyte resistance in PEFCs using electrochemical impedance spectroscopy, J. Electrochem. Soc. 152 (5) (2005) A970.

[73] J.C. Meier, C. Galeano, I. Katsounaros, J. Witte, H.J. Bongard, A.A. Topalov, C. Baldizzone, S. Mezzavilla, F. Schüth, K.J.J. Mayrhofer, Design criteria for stable Pt/C fuel cell catalysts, Beilstein J. Nanotechnol. 5 (2014) 44–67.

[74] J.C. Meier, C. Galeano, I. Katsounaros, A.A. Topalov, A. Kostka, F. Schüth, K.J.J. Mayrhofer, Degradation mechanisms of Pt/C fuel cell catalysts under simulated start–stop conditions, ACS Catal. 2 (5) (2012) 832–843.

[75] S. Maass, F. Finsterwalder, G. Frank, R. Hartmann, C. Merten, Carbon support oxidation in PEM fuel cell cathodes, J. Power Sources 176 (2) (2008) 444–451.

[76] N. Linse, Start/Stop Phenomena in Polymer Electrolyte Fuel Cells (Ph.D. thesis), ETH Zurich, 2012.

[77] H. Schulenburg, B. Schwanitz, N. Linse, G.G. Scherer, A. Wokaun, J. Krbanjevic, R. Grothausmann, I. Manke, 3D imaging of catalyst support corrosion in polymer electrolyte fuel cells, J. Phys. Chem. C 115 (29) (2011) 14236–14243.

[78] A. Kneer, N. Wagner, C. Sadeler, A.-C. Scherzer, D. Gerteisen, Effect of dwell time and scan rate during voltage cycling on catalyst degradation in PEM fuel cells, J. Electrochem. Soc. 165 (10) (2018) F805–F812.

[79] A. Ohma, K. Shinohara, A. Iiyama, T. Yoshida, A. Daimaru, Membrane and catalyst performance targets for automotive fuel cells by FCCJ membrane, catalyst, MEA WG, ECS Trans. 41 (1) (2011) 775–784.

[80] Z. Yang, S. Ball, D. Condit, M. Gummalla, Systematic study on the impact of Pt particle size and operating conditions on PEMFC cathode catalyst durability, J. Electrochem. Soc. 158 (11) (2011) B1439.

[81] Q. Jia, K. Caldwell, K. Strickland, J.M. Ziegelbauer, Z. Liu, Z. Yu, D.E. Ramaker, S. Mukerjee, Improved oxygen reduction activity and durability of dealloyed PtCo$_x$ catalysts for proton exchange membrane fuel cells: Strain, ligand, and particle size effects, ACS Catal. 5 (1) (2015) 176–186.

[82] S. Chen, H.A. Gasteiger, K. Hayakawa, T. Tada, Y. Shao-Horn, Platinum-alloy cathode catalyst degradation in proton exchange membrane fuel cells: Nanometer-scale compositional and morphological changes, J. Electrochem. Soc. 157 (1) (2010) A82.

[83] N.M. Markovic, H.A. Gasteiger, P.N. Ross, Oxygen reduction on platinum low-index single-crystal surfaces in sulfuric acid solution: Rotating ring-Pt(hkl) disk studies, J. Phys. Chem. 99 (11) (1995) 3411–3415.

[84] M.J. Eckl, Y. Mattausch, C.K. Jung, S. Kirsch, L. Schmidt, G. Huebner, J.E. Mueller, L.A. Kibler, T. Jacob, The influence of platinum surface oxidation on the performance of a polymer electrolyte membrane fuel cell—probing changes of catalytically active surface sites on a polycrystalline platinum electrode for the oxygen reduction reaction, Electrochem. Sci. Adv. 2 (3) (2022).

[85] D.J.S. Sandbeck, O. Brummel, K.J.J. Mayrhofer, J. Libuda, I. Katsounaros, S. Cherevko, Dissolution of platinum single crystals in acidic medium, Chemphyschem : A Eur. J. Chem. Phys. Phys. Chem. 20 (22) (2019) 2997–3003.

[86] K. Kodama, A. Motobayashi, A. Shinohara, N. Hasegawa, K. Kudo, R. Jinnouchi, M. Osawa, Y. Morimoto, Effect of the side-chain structure of perfluoro-sulfonic acid ionomers on the oxygen reduction reaction on the surface of Pt, ACS Catal. 8 (1) (2017) 694–700.

[87] K. Kodama, A. Shinohara, R. Jinnouchi, Y. Morimoto, Strategies for designing ideal Pt/Ionomer interfaces in polymer electrolyte fuel cells, R D Rev. Toyota CRDL (49) (2018) 1–11.

[88] J. Huang, J. Zhang, M. Eikerling, Unifying theoretical framework for deciphering the oxygen reduction reaction on platinum, Phys. Chem. Chem. Phys. 20 (17) (2018) 11776–11786.